Periodic bursting cycles on the edge to square duct turbulence

Periodic bursting cycles on the edge to square duct turbulence

Markus Scherer[1,*], **Markus Uhlmann**[1,†], **and Genta Kawahara**[2,‡]

[1]Institute for Hydromechanics, Karlsruhe Institute of Technology, 76131 Karlsruhe, Germany
[2]Graduate School of Engineering Science, Osaka University, 1-3 Machikaneyama, Toyonaka, Osaka 560-8531, Japan

E-mail: [*]markus.scherer@kit.edu, [†]markus.uhlmann@kit.edu, [‡]genta.kawahara.es@osaka-u.ac.jp

Abstract. The long-time behaviour of trajectories embedded in the edge manifold between the laminar and turbulent basins of attraction is investigated in order to identify simple invariant solutions to the Navier-Stokes equations in straight ducts with square cross-section. With the aid of the iterative bisection procedure of Toh and Itano (*J. Fluid Mech.*, vol. 481, 2003, pp. 67-76), we detect three travelling waves that represent attracting 'edge states' within the separatrix and saddles w.r.t. the full state space. All three travelling waves are presumably connected to solutions known in the community. In other situations, the edge states to which trajectories are attracted seem to be invariant periodic cycles that feature a rich dynamics: Along each cycle, the flow oscillates periodically between two flow states, in each of which streamwise vorticity is predominantly residing near one set of parallel walls, while the vortical activity associated to the other pair of opposing walls is markedly reduced. This 'switching' dynamics is accompanied by intermittent bursting-like high-dissipation excursions. While we cannot rigorously prove that the identified periodic cycle is a periodic orbit rather than a finite-precision approximation to a heteroclinic cycle, sound arguments for the former supposition are given. Interestingly, the different phases of the periodic cycle qualitatively resemble a similar 'switching' behaviour observed in (chaotic) marginal turbulence, which suggests that the found periodic cycles could help understanding the characteristic dynamics of duct turbulence at low Reynolds numbers.

1. Introduction

A profound understanding of turbulent fluid motion in straight pipes is of fundamental importance for the design of many industrial processes. Nowadays, much is known about the characteristics of turbulence in pipes with circular cross-section in the transitional and fully-developed regime [1, 2]. Less well understood is, however, the more complicated situation of a duct with square cross-section: In contrast to 'canonical' plane channel and circular pipe flows, the presence of four impermeable bounding walls break the lateral homogeneity of the system and induce a mean secondary flow of Prandtl's second kind [3]. Even though of comparably low amplitude (about $\mathcal{O}(1\%)$ of the bulk velocity u_b), this turbulence-driven secondary motion is well-known to markedly alter the momentum transport and heat transfer normal to the mean flow direction [4]. Previous experiments [5, 6] and direct numerical simulations (DNS) [7–9] therefore investigated the characteristics of the mean secondary flow field, the spatial distribution of the Reynolds stress tensor components, the role of the individual terms in the vorticity transport equation as well as the interplay between secondary currents and thermal convection

[10, 11]. Uhlmann et al. [12] and Pinelli et al. [13], on the other hand, analysed the origin of the mean secondary flow phenomena at the level of individual coherent structures including streamwise velocity streaks and quasi-streamwise vortices, which are elementary ingredients of the self-sustaining regeneration cycle of near-wall turbulence [14–16]. In particular, it was shown that the spatial constraints in form of the four bounding no-slip walls restrict the mobility of individual quasi-streamwise vortices [17] and thus cause the appearance of the characteristic cross-sectional pattern of the mean streamwise vorticity. From a dynamical systems perspective on turbulence [18], the coherent structures embedded in the chaotic turbulent attractor represent low-dimensional, spatiotemporally organised patterns that carry a relevant portion of energy and/or contribute to its dissipation [19]. Within this framework, chaotic turbulence dynamics might be interpreted as a 'pinballing' between individual unstable low-dimensional invariant sets including equilibria (EQ) and periodic orbits (PO) within a high-dimensional state space [20, 21] – a picture that has proven extraordinarily useful in furthering our understanding of sustained turbulence [22, 23] and the transition to turbulence [2, 24]. In square duct flows, several families of travelling waves (TW), which are equilibrium solutions to the Navier-Stokes equations when observed in an appropriate co-moving frame of reference, have been found in the past: The solutions detected by Wedin et al. [25] and Okino et al. [26] can be classified as 'four-vortex states' in that two dominant pairs of vortices residing on two opposite walls characterise the streamwise-averaged secondary flow field. Okino and Nagata [27] later extended their database by a 'two-vortex state' TW which features just a single pair of counter-rotating mean secondary flow vortices at one of the four solid walls. The family of TWs presented by Uhlmann et al. [28], in turn, reveals an 'eight-vortex state' mean secondary flow pattern that possesses a striking similarity to the characteristic long-time averaged secondary flow field of chaotic turbulent trajectories. The 'four-vortex state' of Okino et al. [26], on the other hand, resembles time averages over intermediate intervals of $\mathcal{O}(100)$ bulk time units length at marginal bulk Reynolds numbers $Re_b \equiv u_b H/\nu \approx 1100$, where u_b, ν and H denote the bulk velocity, kinematic viscosity and half the side-length of the square cross-section, respectively (cf. § 2). Uhlmann et al. [12] showed that under such marginal conditions, the cross-section scaled in wall units is too small to accommodate a full turbulent regeneration cycle [14] on each of the four walls, so that the turbulent flow activity is constrained to only two walls facing each other. Note that analogous observations are reported in minimal closed channels, where turbulence activity is often constrainted to one of the two walls [29]. Which pair of parallel walls is currently 'active', though, changes intermittently, so that in the long-time average, the characteristic 'eight-vortex pattern' is recovered even for marginal conditions. While the TW solution of Okino et al. [26] might indeed represent a flow state visited by turbulent trajectories at marginal conditions, the understanding of the dynamics of this 'switching' behaviour remains incomplete. Of particular interest is therefore the identification of time-dependent invariant sets such as – in the simplest case – individual (relative) periodic orbits or groups of saddle TWs that are interconnected by heteroclinic orbits, often termed *heteroclinic cycles* [cf. 30, p. 46ff and 31, p. 631ff].

In the current study, we have isolated several time-recurrent trajectories within the 'edge manifold' (that is, the manifold separating the laminar and turbulent basins of attraction) using the iterative bisection procedure ('edge-tracking') of Toh and Itano [32] (in the following referred to as TI03). In the context of rectangular duct flows, only two previous studies are known to the authors that have performed edge-tracking in their analysis: Biau and Bottaro [33] used it to underline the similarity between the secondary flow patterns of states embedded in the edge manifold and their solutions obtained by an optimisation procedure, without making further efforts to identify invariant solutions along the edge. Okino [34, in Japanese], on the other hand, performed an edge-tracking study for square duct flow in domains of different streamwise period $L_x/H \in \{2\pi, 4\pi, 8\pi\}$. For the three streamwise domain lengths, the edge state was found to be a 'domain-filling' TW solution, a chaotic relative attractor and a spatially localised puff-like TW

solution similar to that found by Avila et al. [35] in a circular pipe, respectively. However, to the best of the authors' knowledge, no time-dependent invariant solution in rectangular duct flow was known prior to the current study, so that we consider the current results to be of significant interest for the understanding of the turbulent dynamics at marginally turbulent conditions.

The manuscript is organised as follows: In § 2, the physical system under consideration as well as the admissible symmetries of the governing equations are described. The different numerical methods that are required to perform an edge-tracking analysis and to later converge simple invariant sets are presented in § 3. The simulation results obtained with the aid of these techniques are discussed in § 4. The manuscript closes with a summary of our findings and a discussion of the 'nature' of the isolated time-recurrent invariant sets in § 5. Specifically, sound arguments will be presented which imply that the trajectories shadow a (relative) periodic orbit rather than a heteroclinic cycle.

2. Theoretical framework

2.1. Flow configuration

In the remainder of this work, we analyse the flow of an incompressible Newtonian fluid in a streamwise periodic duct of square cross-section with side lengths $2H$ and no-slip conditions imposed along the four impermeable walls. The origin of a Cartesian coordinate system is placed in the centre of the cross-section, with its basis vectors pointing in the streamwise (x) and the two cross-stream, wall-normal directions (y, z). The velocity field is denoted by $\boldsymbol{u}(\boldsymbol{x}, t) = (u, v, w)^T$, with u, v and w indicating fluid motion along the x-, y- and z-direction, respectively. The corresponding vorticity field is introduced as $\boldsymbol{\omega}(\boldsymbol{x}, t) \equiv \nabla \times \boldsymbol{u} \equiv (\omega_x, \omega_y, \omega_z)^T$. The flow is driven by a time-dependent streamwise pressure gradient that is adjusted at each time step to ensure a constant mass flow rate Q and thus bulk velocity $u_b \equiv Q/(4H^2)$. Wall shear stress $\tau_w(t)$ and friction velocity $u_\tau(t) = \sqrt{\tau_w(t)/\rho}$ are understood as averages over the duct perimeter. Averaging operators of the form $\langle \bullet \rangle_j$ ($j \in \{x, y, z, t\}$) indicate averaging along one or more spatial directions or time. All simulations performed in the course of this study feature streamwise-periodic domains with fundamental period $L_x = 2\pi H$ (with $\alpha \equiv 2\pi/L_x = 1/H$ denoting the fundamental wavenumber), which is for all considered Reynolds numbers markedly larger than the minimal streamwise domain length $(L_x^+)_{min} \approx 200$ required to sustain turbulence in a square duct [12]. Here, the notation $\bullet^+$ indicates scaling in wall units, that is, non-dimensionalisation using $\langle u_\tau \rangle_t$ and ν. Throughout, time is measured in bulk time units $T_b = H/u_b$.

2.2. Symmetric subspaces

Subject to the given boundary conditions, the Navier-Stokes system allows for a number of continuous and discrete symmetries. The streamwise periodicity of the domain leads to a continuous translational symmetry in x, viz.

$$l_x(s_x): \quad [u, v, w]\,(x, y, z) \quad \rightarrow \quad [u, v, w]\,(x + s_x, y, z) \qquad \forall\, s_x \in \left[-\frac{\pi}{\alpha}, \frac{\pi}{\alpha}\right), \tag{1}$$

that allows for the existence of travelling waves (relative equilibria) and relative periodic orbits, where 'relative' refers to invariance within a co-moving frame of reference. In contrast to pipes with circular cross-section, the boundary conditions in the square duct case break the continuous azimuthal rotational symmetry and reduce it to the discrete dihedral group D_4. For the sake of generality, we restrict ourselves in the following sections to the elements of the dihedral symmetry group $D_2 = \{e, \mathbf{Z}_y, \mathbf{Z}_z, \mathbf{R}_\pi\}$ which is also fulfilled in ducts with rectangular cross-section (with e denoting the identity). The two reflectional symmetries $\mathbf{Z}_y, \mathbf{Z}_z$ and the π-rotational symmetry

$\mathbf{R}_\pi$ contained in D_2 are defined as

$$\left.\begin{aligned} \mathbf{Z}_y: \quad [u,v,w]\,(x,y,z) &\rightarrow [u,-v,w]\,(x,-y,z) \\ \mathbf{Z}_z: \quad [u,v,w]\,(x,y,z) &\rightarrow [u,v,-w]\,(x,y,-z) \\ \mathbf{R}_\pi: \quad [u,v,w]\,(x,y,z) &\rightarrow [u,-v,-w]\,(x,-y,-z) \end{aligned}\right\}. \tag{2}$$

The governing equations are thus equivariant under the symmetry group $\Gamma = SO(2)_x \times D_2$. In the current work, the following subgroups of Γ for specific streamwise shifts are of specific interest and therefore merit a separate definition:

$$\left.\begin{aligned} \mathbf{S}_y: \quad [u,v,w]\,(x,y,z) &\rightarrow [u,-v,w]\left(x+\frac{\pi}{\alpha},-y,z\right) \\ \mathbf{S}_z: \quad [u,v,w]\,(x,y,z) &\rightarrow [u,v,-w]\left(x+\frac{\pi}{\alpha},y,-z\right) \\ \mathbf{\Omega}_\pi: \quad [u,v,w]\,(x,y,z) &\rightarrow [u,-v,-w]\left(x+\frac{\pi}{\alpha},-y,-z\right) \end{aligned}\right\}. \tag{3}$$

3. Numerical method

3.1. Fluid solver

The Navier-Stokes equations are integrated using a pseudo-spectral method in primitive variable formulation for the spatial derivatives together with a fractional step method and a mixed explicit-implicit time marching scheme [cf. 13 for a detailed overview]. The velocity and pressure fields are expanded in terms of truncated Fourier series in the periodic streamwise direction and Chebyshev polynomials in the two cross-stream directions. Gauss-Chebyshev-Lobatto points are chosen as collocation points in the cross-stream directions, whereas a grid of equispaced nodes is used in the streamwise direction. In the current simulations, fields are expanded by $N_x = 64$ Fourier modes in the streamwise direction and between $N_y = N_z = 65$ and $N_y = N_z = 129$ Chebyshev polynomials in the cross-stream directions, ensuring that the grid spacing fulfills $\Delta x^+ \leq 14$ and $\max(\Delta y^+), \max(\Delta z^+) \leq 3.5$ in all considered cases. In the streamwise homogeneous direction, back and forth transformation between physical and Fourier space is performed based on fast Fourier transforms (FFT), taking into account de-aliasing according to the 2/3-rule. Poisson and Helmholtz problems arising from the numerical discretisation are solved in Fourier space for each streamwise wavenumber separately with the aid of a fast-diagonalisation technique [36], whereas nonlinear contributions are solved in physical space. The time integration scheme combines a semi-implicit treatment of the viscous terms with an explicit three-step low-storage Runge-Kutta method for the remaining ones [37, 38]. Throughout, the time step is chosen small enough to keep the CFL number below 0.3.

3.2. Newton-GMRES hookstep algorithm

To converge nearly recurrent episodes within a DNS trajectory to a truly invariant set such as a TW or a PO, a Newton-Raphson shooting method is used within the high-dimensional state space spanned by the coefficients of the Fourier-Chebyshev-Chebyshev expansion. The linear system arising in this context is approximately solved by a variant of the generalised minimal residual (GMRES) algorithm of Saad and Schultz [39] [cf. 40 for a detailed overview]. Since a straight Newton-GMRES procedure is typically not sufficient for convergence [41], the size of the determined Newton step is afterwards restricted to the region in which the linearisation is a sufficiently good approximation to the functional using the 'hookstep' procedure outlined by Dennis and Schnabel [42]. In the past, this combined Newton-GMRES-hookstep approach has been proven suitable to converge solutions even in high-dimensional state spaces [41, 43]. The general structure of the current implementation follows to a large extent that in the

`Openpipeflow` code of Willis [44], but represents an independently developed code whose core is the DNS solver described in section 3.1. To validate the implementation, we have successfully re-converged one of the upper-branch TW solutions found in Uhlmann et al. [28].

3.3. Edge-tracking

The iterative 'edge-tracking' algorithm of TI03 is a repeated bisection procedure that identifies numerical trajectories within the edge manifold $\mathscr{M}$ that separates the laminar and turbulent basins of attraction [45]. For the ith time interval, a parameter $\beta_i \in \mathbb{R}$ ($\forall i \in \mathbb{N}$) is sought that rescales the perturbation of a given flow state $\boldsymbol{u}_{i-1}(\boldsymbol{x}, t_{i-1})$ w.r.t. the laminar base flow $\boldsymbol{u}_{lam}(y,z) = (u_{lam}, 0, 0)^T$ at the beginning of each iteration interval t_{i-1} as

$$\begin{cases} \boldsymbol{u}_{\beta_i}(\boldsymbol{x}, t_{i-1}) \equiv \boldsymbol{u}_{lam}(y,z) + \beta_i \left(\boldsymbol{u}_{i-1}(\boldsymbol{x}, t_{i-1}) - \boldsymbol{u}_{lam}(y,z)\right) & \text{at } t = t_{i-1} \\ \boldsymbol{u}_{\beta_i}(\boldsymbol{x}, t) \equiv \boldsymbol{u}_{\beta_i}(\boldsymbol{x}, t_{i-1}) + \int_{t'=t_{i-1}}^{t} \partial_t \boldsymbol{u} \, \mathrm{d}t' & \forall t \in (t_{i-1}, t_i) \end{cases} \tag{4}$$

to ensure that the initial condition is located on $\mathscr{M}$. Here, the laminar base flow $\boldsymbol{u}_{lam}(y,z)$ is determined from the Poisson equation $(\partial_{,yy} + \partial_{,zz}) u_{lam} = -\Pi/\nu$, where Π is the constant driving pressure gradient required to maintain a laminar flow with identical mass flow rate Q.

In practice, in each bisection step, a flow trajectory is integrated forward in time according to equation (4) using the DNS code outlined in section 3.1 until it either relaminarises or leaves $\mathscr{M}$ towards the turbulent basin of attraction. The interval in which β_i is expected is then halved with the lower and upper limits representing values that cause the flow to relaminarise and to become fully turbulent, respectively. As an indicator for when a trajectory does no longer reside on the edge manifold $\mathscr{M}$, we monitor the root mean square (r.m.s.) values of the kinetic energy residing in the streamwise-dependent Fourier modes, viz.

$$E_{rms} \equiv \sum_j [E_{3D}]_j^{1/2} \quad \text{with} \quad [E_{3D}]_j = \sum_{i=1}^{N_x} \iint_{y,z=-H}^{H} [\hat{\boldsymbol{u}}_i]_j [\hat{\boldsymbol{u}}_i^*]_j \, \mathrm{d}z\mathrm{d}y \quad \forall j \in \{x, y, z\}, \tag{5}$$

where $\hat{\boldsymbol{u}}_i$ and $\hat{\boldsymbol{u}}_i^*$ denote the ith Fourier coefficient and its complex conjugate, respectively. The notation $[\bullet]_j$ indicates the jth component of a scalar or vector (field). The trajectory is considered as deviated to either of the two basins of attraction when the energy E_{rms}/u_b either drops below $E^l_{rms}/u_b \approx 2 \cdot 10^{-3}$ or, after a rapid energy growth, exceeds $E^t_{rms}/u_b \approx 2 \cdot 10^{-1}$.

Even though each bisection is continued until β_i has been determined up to 14 digits, the exponential growth of the remaining deviation makes an iterative procedure including a re-computation of β_i after $\mathcal{O}(100 T_b)$ typically unavoidable [32, 45]. In the current work, the initial condition for the first iteration $i = 1$ is a flow state $\boldsymbol{u}_0(\boldsymbol{x}, t_0)$ randomly chosen from a fully-turbulent trajectory. The first parameter value β_1 is then clearly smaller than unity. After β_i has been determined up to the desired precision, the next iteration $i+1$ is initiated with a flow field taken from the previous edge trajectory $\boldsymbol{u}_i(\boldsymbol{x}, t_i) \equiv \boldsymbol{u}_{\beta_i}(\boldsymbol{x}, t_{i-1} + \delta t)$, where the interval for re-initialisation is with $\delta t \approx 340 T_b$ of comparable size as in TI03. Due to the iterative procedure with intermittent restarts, the obtained curve is only piecewise continuous, with discontinuities occurring at times t_i and is thus no solution of the Navier-Stokes equations in a strict sense. For the sake of consistency, we follow TI03 and use the expression 'chain solution' for the resulting object. Even though the 'chain solution' itself is not a continuous solution trajectory of the governing equations, we can assume that a continuous trajectory that lies in $\mathscr{M}$ exists for all times and that for the current choice of δt, the 'chain solution' represents a valid approximation to the latter. The fact that the deviation between two consecutive parameter values at the time interval boundaries is seen to be small (β_i is close to unity $\forall i \geq 2$) gives us some confidence that this is indeed the case.

Table 1. List of travelling wave solutions that are identified as edge states with their respective phase velocity c_x. Note that the TW solutions obey more symmetries than the symmetric subspaces in which the edge trajectories are sought - these 'additional' symmetries are enclosed in round brackets. All solutions have been converged using the Newton-GMRES solver outlined in section 3.2 with $[N_x \times N_y \times N_z] = [64 \times 65 \times 65]$ Fourier-Chebyshev-Chebyshev modes.

Case	Re_b	c_x/u_b	Symmetries	(Suspected) corresponding TW
TW_1	1400	1.61	$\mathbf{R}_\pi$,$\mathbf{S}_y$,$\mathbf{S}_z$,($\mathbf{D}_{yz}$),($\mathbf{D}_{zy}$)	'eight-vortex state', Uhlmann et al. [28]
TW_2	2000	1.74	$\mathbf{Z}_y$,($\mathbf{\Omega}_\pi$),($\mathbf{S}_z$)	'four-vortex state', Wedin et al. [25]
TW_3	3200	1.62	$\mathbf{R}_\pi$,($\mathbf{S}_y$),($\mathbf{S}_z$)	'four-vortex state', Okino [34]

4. Results

In the current study, we have analysed the behaviour of trajectories along the edge manifold in different symmetric subspaces. For some of those systems, we repeated the edge tracking procedure for varying Reynolds numbers to scrutinise the impact of the latter on the type of the identified edge states. In the following two sections, we will discuss some selected cases for which the edge trajectories reveal particularly interesting dynamics in that they are attracted by simple, non-chaotic invariant sets such as TWs or periodic cycles.

4.1. Travelling waves

First, we discuss edge trajectories in three different symmetric subspaces for different Reynolds numbers that are attracted by travelling waves. These latter represent saddles in the full state space, but take the role of purely attracting sets within $\mathscr{M}$. The three considered cases TW_1, TW_2 and TW_3 are listed in table 1, together with the respective Reynolds numbers and symmetries. Figure 1(*a-c*) shows the variation of the r.m.s. kinetic energy E_{rms} as the trajectories approach the relative attractors: After an initial apparently chaotic transient of varying length, all three trajectories enter the basin of attraction of the respective TW. Flow states extracted from the respective trajectories in these 'plateau regimes' represent excellent initial guesses for the Newton-GMRES solver and can be converged to truly invariant sets within few Newton iterations. Figure 1(*d-f*) visualises the spatial structure of the three travelling wave solutions in terms of their (exact) coherent structures: Isosurfaces of the streamwise velocity indicate the position of elongated streaks along the no-slip walls, while quasi-streamwise vortices are identified by regions of intense streamwise vorticity. Further informations including the relative phase speed c_x/u_b and the symmetries that the different 'edge states' fulfill are provided in table 1. In this context, it is noteworthy that all edge trajectories approach invariant sets that are located in even higher-symmetric subspaces than those in which the trajectories are searched for. So, TW_1 reveals in addition to the previously defined symmetry group additional reflectional symmetries w.r.t. the diagonals $y = z$ and $y = -z$, viz.

$$\left.\begin{aligned} \mathbf{D}_{yz}: \quad & [u,v,w]\,(x,y,z) \quad \rightarrow \quad [u,w,v]\,(x,z,y) \\ \mathbf{D}_{zy}: \quad & [u,v,w]\,(x,y,z) \quad \rightarrow \quad [u,-w,-v]\,(x,-z,-y) \end{aligned}\right\}. \tag{6}$$

While all three TWs are propagating in positive x-direction at comparable phase speeds $c_x/u_b \in [1.6, 1.75]$, the spatial organisation of their flow fields is markedly different: TW_1 shown in figure 1(*a,d*) features low-speed streaks and a staggered arrangement of counter-rotating quasi-streamwise vortices along each of the four walls. In TW_2 and TW_3 (cf. figure 1(*b,e*) and (*c,f*), respectively), on the other hand, marked elongated streaks accompanied by pairs of

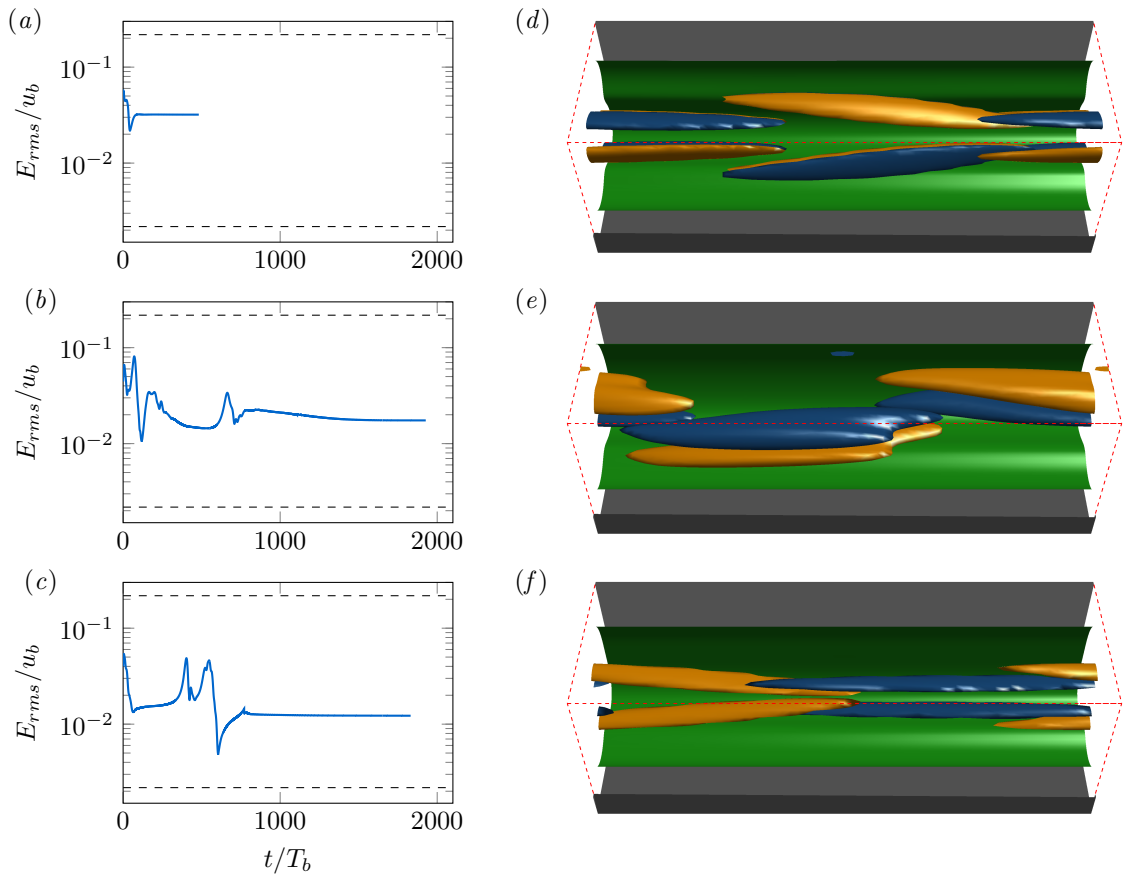

Figure 1. Edge trajectories that are attracted by a travelling wave solution. (*a-c*) Time evolution of the r.m.s. energy signal $E_{rms}(t)$ for varying Reynolds numbers and symmetry groups: (*a*) $Re_b = 1400$, $S = \{e, \mathbf{R}_\pi, \mathbf{S}_y, \mathbf{S}_z\}$, TW_1; (*b*) $Re_b = 2000$, $S = \{e, \mathbf{Z}_y\}$, TW_2; (*c*) $Re_b = 3200$, $S = \{e, \mathbf{R}_\pi\}$, TW_3. See table 1 for the 'additional' symmetries fulfilled by the TW solutions. Horizontal dashed lines indicate the limits above (below) which a trajectory is considered as turbulent (laminar). Shown is only the time up to the flow state that was used as initial condition for the Newton-GMRES iteration. (*d-f*) Three-dimensional visualisations of the converged TW 'edge states' in (*a-c*). Shown are isosurfaces of the streamwise velocity $u = 0.55\max(|u|)$ (green) and isocontours of the streamwise vorticity $\omega_x = \pm 0.55\max(|\omega_x|)$ (clockwise/counter-clockwise rotation indicated by orange/blue color), with mean flow from left to right. For the sake of visualisation, the two frontal walls are not shown and the isocontour of u is visualised for $y \leq -z$ only.

counter-rotating vortices are identified near two of the four walls only. A comparison of the converged TWs with those known in the community reveals that TW_1 belongs to the family of lower-branch 'eight-vortex solutions' of Uhlmann et al. [28] (compare the visualisation in their fig. 5 for identical conditions $Re_b = 1400$ and $\alpha H = 1$). The remaining two travelling wave solutions, TW_2 and TW_3, are assumed to be connected to the solution branches identified by Wedin et al. [25] on the one hand and Okino et al. [46] and Okino [34] on the other hand. In both cases, the mean secondary flow field is a 'four-vortex state' with two pairs of counter-rotating vortices associated with two walls facing each other. But since the current domain size and Reynolds numbers do not coincide with those in these studies, branch continuation in the parameter space spanned by Re_b and αH would be necessary to prove that the converged TWs

Table 2. List of attracting periodic cycles identified as edge states together with the asymmetric chaotic relative attractor. For the cycles, the estimated period T is determined as the value to which the sequences T^k_{min} and T^k_{max} converge for $t \to \infty$. The last column indicates which of the four triangular sectors Ω_i (cf. equation (9)) contribute (at least temporarily) a significant portion of streamwise vorticity to the overall budget.

Case	Re_b	T/T_b	Symmetries	'active' sections
$\mathrm{PC2200}_y$	2200	≈ 592	$\mathbf{Z}_y$	$\Omega_W, \Omega_N/\Omega_S$
$\mathrm{PC2400}_y$	2400	653.2	$\mathbf{Z}_y$	$\Omega_W, \Omega_N/\Omega_S$
$\mathrm{PC3200}_{yz}$	3200	563.8	$\mathbf{Z}_y$,$\mathbf{Z}_z$	$\Omega_W/\Omega_E, \Omega_N/\Omega_S$
CA3200	3200	-	-	all

indeed belong to the same family of solutions. Such a continuation campaign is beyond the scope of the current study and is left for future investigations. Nonetheless, supposing that the solution families are indeed the same, the current results imply that most of the currently known TW solutions in square duct flow take the role of 'edge states' in appropriate symmetric subspaces [compare the discussion for circular pipe flow in 45 and 47]. Note that this is not necessarily to be expected *a priori* as all previously known solution families have been identified by homotopy and back-continuation from either externally forced or internally heated systems [22], without an *a priori* guarantee that these solutions are indeed visited by chaotic flow trajectories.

4.2. Quasi-periodic cycles

We now turn our attention to situations in which the analysed edge trajectories are observed to approach time-dependent invariant sets that seem to be limit cycles in $\mathscr{M}$. Among these cases that are listed in table 2, cases $\mathrm{PC2200}_y$ and $\mathrm{PC2400}_y$ feature only a single reflectional symmetry $\mathbf{Z}_y$ and differ solely by the Reynolds number, whereas case $\mathrm{PC3200}_{yz}$ simultaneously obeys the two reflectional symmetries $\mathbf{Z}_y$ and $\mathbf{Z}_z$. As a reference, table 2 also contains case CA3200, which does not fulfill any symmetry other than the identity $S = \{e\}$ and reveals a chaotic behaviour throughout the observation interval. Before discussing the dynamics in more detail, let us remark that the systems with a single reflectional symmetry $\mathbf{Z}_y$ are seen to approach a TW solution at $Re_b = 2000$, while the edge states detected for higher Reynolds numbers $Re_b \gtrsim 2200$ are all periodic cycles. Clearly, conclusions based on single phase space trajectories have to be drawn with caution, as $\mathscr{M}$ might be of very complex shape and feature a variety of different edge states. Nonetheless, it can be speculated whether the observed (relative) attracting cycles are connected to TW_2 by some global bifurcation.

The quasi-periodic dynamics of the 'chain solution' in cases $\mathrm{PC2400}_y$ and $\mathrm{PC3200}_{yz}$ are clearly visible in the time evolution of the r.m.s. energy signal presented in figure 2(*a,c*), respectively. For both cases, relatively quiet periods alternate with intermittently occurring bursting events, during which the streamwise-dependent Fourier modes record, temporarily, a significant gain of energy. The length of the individual bursting sequences is visually much shorter than a full recurrence period. At first glance, the fundamental period of case $\mathrm{PC2400}_y$ seems to be at least twice as long as the one in case $\mathrm{PC3200}_{yz}$, but featuring two energetic peaks of different amplitude per cycle. As we shall see later, both cycles 'oscillate' between two different flow states, in which vorticity is either concentrated near the walls at $y/H \in \{-1, 1\}$ or those at $z/H \in \{-1, 1\}$. The difference is that for case $\mathrm{PC3200}_{yz}$, these two states are found to be identical modulo a rotation by $\pi/2$ about the x-axis, so that both states are indistinguishable in terms of the energy signal. In fact, the global kinetic energy evolution is in the pressure-driven

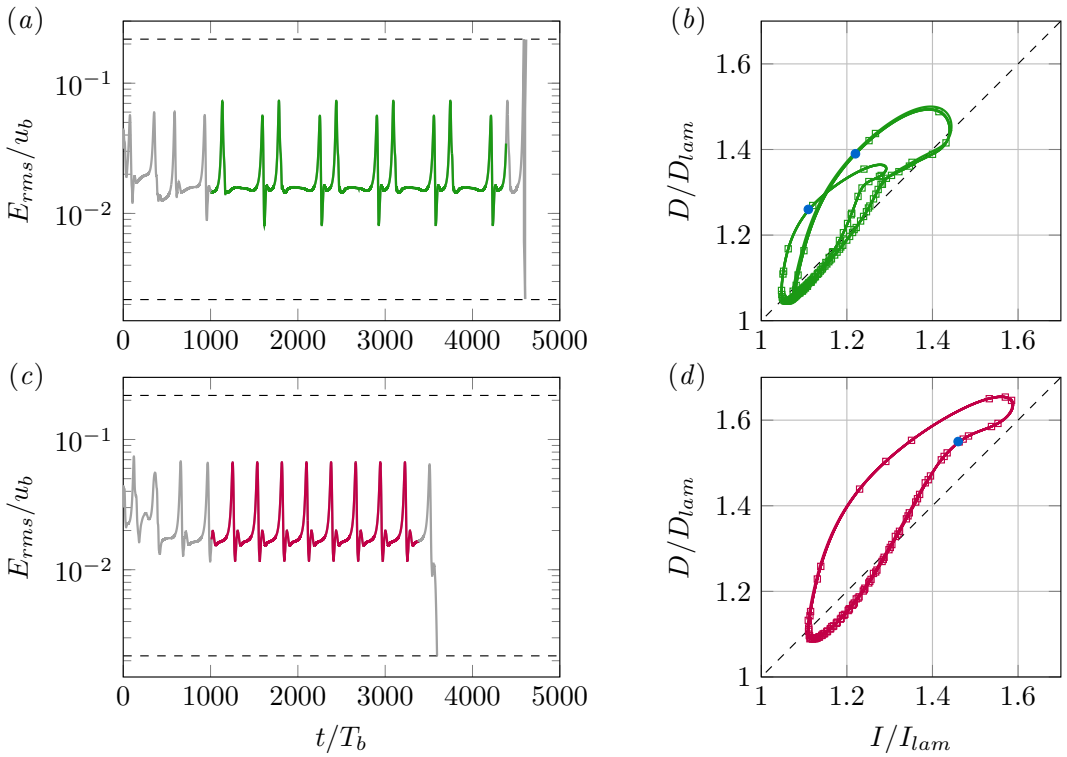

Figure 2. Time evolution of energy and dissipation along the edge trajectories (*a,b*) $\mathrm{PC2400}_y$ and (*c,d*) $\mathrm{PC3200}_{yz}$ that are attracted by a periodic cycle. (*a,c*) Time evolution of the r.m.s. energy signal $E_{rms}(t)$. The time interval, during which the dynamics along the 'chain solution' can be considered as essentially periodic, is highlighted. (*b,d*) Two-dimensional projection of the trajectory dynamics onto a plane spanned by the global dissipation D and energy input rate I. Both quantities are normalised with the respective values in a laminar flow at identical mass flow rate Q, i.e. $D_{lam} = I_{lam}$. Open square symbols are placed along the curves in time intervals of $\approx 25T_b$ length to give an impression of how 'fast' D and I change along the curve. Note that only the time interval highlighted in (*a,c*) is shown in the (D,I)-diagram, with blue dots marking when the snapshots shown in figure 4 have been extracted.

square duct flow fully described by a simple balance between energy input I and dissipation D, viz.

$$\frac{\mathrm{d}E}{\mathrm{d}t} = I - D, \tag{7}$$

where

$$E = \frac{1}{2|V|}\int_\Omega ||\boldsymbol{u}||^2 \,\mathrm{d}\boldsymbol{x}, \quad I = -\frac{1}{|V|}\int_\Omega \partial_x\left(\frac{pu}{\rho}\right) + \Pi_t u \,\mathrm{d}\boldsymbol{x}, \quad D = \frac{1}{|V|}\int_\Omega \nu||\boldsymbol{\omega}||^2 \,\mathrm{d}\boldsymbol{x}$$

with $\Omega = [0, 2\pi/\alpha) \times [-H, H] \times [-H, H]$, $V = 8\pi H^2/\alpha$ and the time varying driving streamwise pressure gradient Π_t. In the classical energy input-dissipation diagrams in figure 2(*b,d*), the bursting phases in the energy signal manifest themselves as high-dissipation excursions from the more quiescent regions close to the laminar attractor at (D_{lam}, I_{lam}). In the two-dimensional projection onto the (D, I)-plane, the state space trajectories of the 'chain solution' collapse almost perfectly onto two closed cycles. These latter are oriented in such a way that wandering

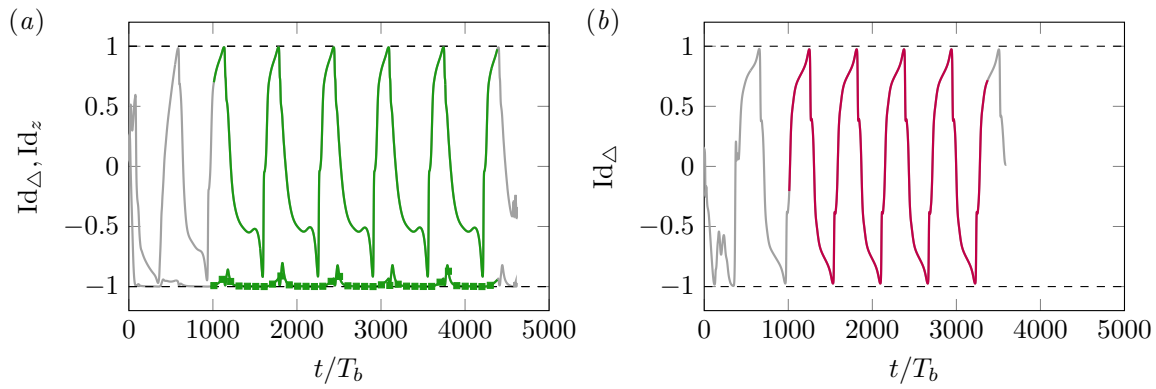

Figure 3. Time evolution of the indicator functions $\mathrm{Id}_\triangle$ (—) and Id_z (–■–) as defined in equations (8) and (10), respectively, for cases (*a*) $\mathrm{PC2400}_y$ and (*b*) $\mathrm{PC3200}_{yz}$.

along the 'chain solution' as $t \to \infty$ means orbiting along the curve in the (D, I)-plane in clockwise sense. In other words, each bursting phase starts with a rapid increase in dissipation, followed by an intensification of the wall friction and thus the external energy input I with a small time lag of $\mathcal{O}(10^0 T_b)$ length. This characteristic behaviour is consistent with the classical concept of the self-sustaining interaction process between streamwise velocity streaks and quasi-streamwise vortices in the buffer layer of turbulent flows [14, 15] and has been reported for periodic orbits [48] and quasi-periodic cycles [32] in various flow configurations.

In accordance with the earlier discussed qualitatively different evolution of E_{rms} for cases $\mathrm{PC2400}_y$ and $\mathrm{PC3200}_{yz}$, the (D, I)-projection of the latter case collapses onto a single bean-like loop, whereas $\mathrm{PC2400}_y$ follows a more complicated, double loop orbit. Again, this qualitative difference originates in the fact that both trajectories oscillate between two flow states, but in case $\mathrm{PC3200}_{yz}$ the two states are identical modulo a rotation by $\pi/2$ in the cross-section, such that the two bursting loops collapse onto a single one in the two-dimensional projection. Before discussing the alternating flow states in more detail, let us come back to the different time scales in the periodic 'chain-solution'. As indicated by the square symbols placed in time intervals of about $\approx 25 T_b$ along the curves in figure 2(*b*,*d*), the 'speed' at which the flow orbits along the (D, I)-curve varies significantly in the plane: Both 'chain solutions' spend a considerable fraction of the period in the more quiescent regions at low values of D and I, with I slightly exceeding the values attained by D. On the other hand, they quickly pass the high-dissipation sequences during which $D > I$. Note that this is inasmuch expected as $\langle D \rangle_t = \langle I \rangle_t$ must hold for sufficiently long time intervals, where $\langle \bullet \rangle_t$ indicates long-time averages along a single flow trajectory.

In order to quantify the foreshadowed intermittent 'switching' between two different flow states, we determine a dimensionless indicator function [12]

$$\mathrm{Id}_\triangle \equiv \frac{(S_N + S_S) - (S_W + S_E)}{S_N + S_S + S_W + S_E}, \tag{8}$$

with

$$\left.\begin{aligned} S_i &= \int_{\Omega_i} \langle \omega_x \rangle_x^2 \, \mathrm{d}A \qquad \forall i \in \{W, S, E, N\}, \\ \Omega_S &= \{(y,z) |\ y < z \ \wedge\ y < -z\}, \quad \Omega_N = \{(y,z) |\ y > z \ \wedge\ y > -z\}, \\ \Omega_W &= \{(y,z) |\ y > z \ \wedge\ y < -z\}, \quad \Omega_E = \{(y,z) |\ y < z \ \wedge\ y > -z\}, \end{aligned}\right\}. \tag{9}$$

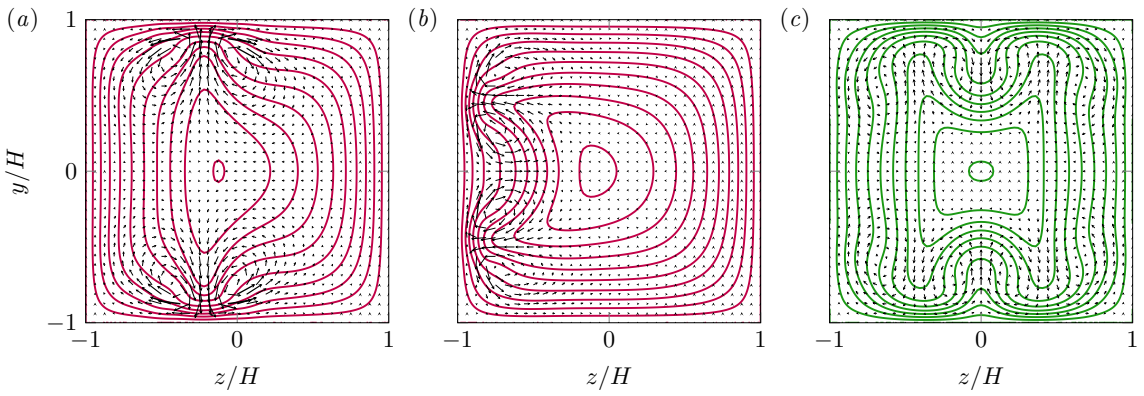

Figure 4. Instantaneous snapshots of the streamwise-averaged primary and secondary flow field $\langle u\rangle_x$ and $(\langle v\rangle_x, \langle w\rangle_x)^T$ for cases (a,b) PC2400$_y$ and (c) PC3200$_{yz}$. Solid lines represent isolevels of $\langle u\rangle_x/u_b$ between 0 and 2, with an increment of 0.2. The intensity and orientation of the secondary flow field $(\langle v\rangle_x/u_b, \langle w\rangle_x/u_b)^T$ is indicated by the vector plot. Note that the arrow scaling differs between (a,b) and (c). The presented snapshots have been extracted from the respective 'chain solutions' at (a) $t = 2440T_b$, $(D/D_{lam}, I/I_{lam}) = (1.39, 1.22)$; (b) $t = 2905T_b$, $(D/D_{lam}, I/I_{lam}) = (1.26, 1.11)$; (c) $t = 2409T_b$ and $t = 2409 \pm 281.9T_b$ (when rotated by $\pi/2$ about the x-axis), $(D/D_{lam}, I/I_{lam}) = (1.55, 1.46)$.

Thus, by definition, $\mathrm{Id}_\triangle$ attains a value close to plus (minus) unity when the enstrophy carried by the streamwise vorticity is predominantly focussed near the walls at $y \in \{-H, H\}$ (the walls at $z \in \{-H, H\}$), respectively. In addition, we introduce the analogously defined indicator functions

$$\mathrm{Id}_y \equiv \frac{S_N - S_S}{S_N + S_S} \quad \text{and} \quad \mathrm{Id}_z \equiv \frac{S_E - S_W}{S_E + S_W}, \tag{10}$$

where Id_y (Id_z) indicates, if close to unity, that vorticity is mainly concentrated near the wall at $y = H$ ($z = H$), or near that at $y = -H$ ($z = -H$) for values close to negative unity.

In figure 3(a,b), $\mathrm{Id}_\triangle$ is evaluated for cases PC2400$_y$ and PC3200$_{yz}$, while Id_y is trivially zero in both cases and Id_z at least in the latter case as a consequence of the enforced symmetries. The curves associated with $\mathrm{Id}_\triangle$ clearly indicate that the dynamics of both systems are characterised by periodic oscillations between two states in which streamwise enstrophy predominantly resides near one pair of parallel walls, while vortical activity is much weaker in the vicinity of the remaining two walls. In contrast to case PC3200$_{yz}$, however, Id_z is close to minus unity over the entire observation interval of case PC2400$_y$, indicating that the wall at $z = -H$ features a much stronger vortical activity than its counterpart at $z = H$. Figure 4 supports this observation by showing the streamwise-averaged flow field for selected snapshots along the 'chain solution' that are representative of either of the two flow states. The extracted snapshots are characterised by a comparably high dissipation (see the blue dots in figure 2(b,d)) and feature between one and two streak-vortex pairs per 'active' wall, with lateral extents $\delta z^+ = \mathcal{O}(10)$ comparable to those typically observed for the quasi-streamwise vortices of the buffer layer in canonical channel [29, 49] and square duct flows [12, 13].

The time signal $\mathrm{Id}_\triangle(t)$ is moreover a good candidate to estimate the fundamental period of the shadowed limit cycles. To this end, we measure the recurrence time of the 'chain solutions' based on the time interval between two consecutive maxima or minima of $\mathrm{Id}_\triangle(t)$ as

$$T^k_{max} = t^{k+1}_{max} - t^k_{max} \quad \text{and} \quad T^k_{min} = t^{k+1}_{min} - t^k_{min}, \tag{11}$$

respectively, where t^k_{max} (t^k_{min}) corresponds to the time at which $\mathrm{Id}_\triangle(t)$ attains its kth global maximum (minimum). Note that the thereby estimated value for the cycle period can at most be determined up to a precision of $5\Delta t \approx 0.07T_b$, which is half the interval in which statistics have been stored to disk alongside the simulation runs. The sequence of values attained by T^k_{max} and T^k_{min} for increasing k presented in figure 5 underlines that the estimated period converges within a few cycles to essentially constant values $T \approx 653.2T_b$ ($\mathrm{PC2400}_y$) and $T \approx 563.8T_b$ ($\mathrm{PC3200}_{yz}$), providing clear evidence that the two edge trajectories indeed approach a limit cycle (within $\mathscr{M}$) with finite period. To quantify the deviation of the 'chain solution' from a truly closed cycle, we evaluate in the following the kinetic energy of the residual flow field

$$\delta\boldsymbol{u}(\boldsymbol{x}, t, \boldsymbol{\delta}, \delta t) = \boldsymbol{u}(\boldsymbol{x}, t) - \boldsymbol{u}(\boldsymbol{x} - \boldsymbol{\delta}, t + \delta t), \tag{12}$$

where $\boldsymbol{\delta} = (s_x, 0, 0)^T$ denotes a spatial shift in the streamwise direction and $\delta t \in \mathbb{R}$ is a shift in time. Defining the kinetic energy contained in the jth velocity component as

$$E_j(\boldsymbol{u}) = \frac{1}{|V|}\int_\Omega [\boldsymbol{u}(\boldsymbol{x}, t)]_j^2 \,\mathrm{d}\boldsymbol{x} \quad \text{with} \quad j \in \{x, y, z\}, \tag{13}$$

we can eventually express the relative error in terms of the kinetic energy for the jth velocity component as [32]

$$\hat{E}_j(\boldsymbol{u}, t, \delta t) = \frac{\min_{s_x} E_j(\delta\boldsymbol{u}(\boldsymbol{x}, t, s_x, \delta t))}{E_j(\boldsymbol{u}(\boldsymbol{x}, t))} \quad \text{with} \quad j \in \{x, y, z\}. \tag{14}$$

Note that minimisation over all possible streamwise shifts is necessary, since the phase velocity is *a priori* unknown. In practice, the minimisation is performed over discrete shifts s_x at increasingly fine discretisation in the context of a standard bisection procedure. Using the values to which the series T_{max} and T_{min} converged as guesses for the period T, we have evaluated the relative error $\hat{E}_j(\boldsymbol{u}, t, T)$ for all three velocity components at different times t along the 'chain solution'. Despite the fact that the latter is just an approximation to an actual edge trajectory and notwithstanding the long period that makes an intermediate re-iteration of β_i unavoidable, $\hat{E}_j(\boldsymbol{u}, t, T)$ is for case $\mathrm{PC2400}_y$ at most $\mathcal{O}(10^{-5})$ for any of the three velocity components. For case $\mathrm{PC3200}_{yz}$, taking into account that the Navier-Stokes equations in square duct flow are equivariant under rotations by $m\pi/2$ ($m \in \mathbb{Z}$) about the x-axis, the deviation is found to be at most $\mathcal{O}(10^{-5})$ for both, the 'full' period $T = 563.8T_b$ and half its value.

5. Discussion and Conclusion

In the previous sections, we have studied the flow in a streamwise periodic duct with square cross-section from a dynamical systems point of view. When artificially forced to stay within the 'edge manifold' $\mathscr{M}$ that separates the laminar and turbulent basins of attraction under additional symmetric constraints, trajectories are found to be attracted by simple invariant sets in phase space, including TWs and periodic cycles. While all TW solutions that take the role of edge states in the considered subspaces are known [25, 28, 34], no comparable periodic limit cycles have been detected before in a square duct. In plane Poiseuille flow, however, a structurally similar phase space object was detected in the pioneering work of TI03 with the same numerical bisection technique as in the current work. TI03 discussed in detail that the observed relatively attracting cycle could be both, a periodic orbit or a heteroclinic cycle. Indeed, it has been shown that structurally stable heteroclinic cycles can exist in systems with symmetry group $S = O(2)$ such as plane Poiseuille flow [50] and there have been some attempts to interpret turbulent bursting events as heteroclinic cycles [51, 52]. However, limited computational resources hindered TI03

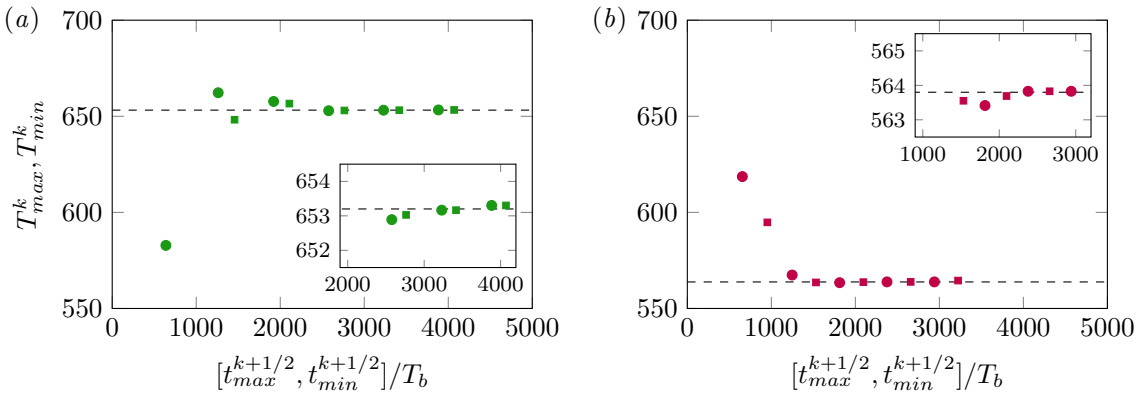

Figure 5. Time evolution of the estimated cycle period determined from the time intervals between two consecutive extrema of $\mathrm{Id}_\triangle$ using equation (11) for cases (a) $\mathrm{PC2400}_y$ and (b) $\mathrm{PC3200}_{yz}$. Here, we associate each value of the estimated period with the midpoint of the time interval based on which it has been determined, i.e. $t_\bullet^{k+1/2} = (t_\bullet^k + t_\bullet^{k+1})/2$. Squares and circles represent the kth cycle turn-over time estimated based on the maxima (T_{max}) and minima (T_{min}) of $\mathrm{Id}_\triangle$, respectively. Dashed lines indicate values (a) $653.2T_b$ and (b) $563.8T_b$, respectively. The insets show close-ups of the same data close to the estimated period length.

from tracking their 'chain solution' around the cyclic orbit for more than one and a half periods and thus from clarifying the type of invariant set that it is shadowing.

For the square duct, the authors are not aware of a comparable statement on the existence of structurally stable heteroclinic cycles under the changed symmetry conditions. Also, the 'chain solution' found by TI03 in the closed channel spends a considerable amount of time near two selected points in the (D, I)-plane that are almost in equilibrium ($I \approx D$), which motivated the speculation that their 'chain solution' is visiting the neighbourhood of two saddle-node travelling waves. In our case, the 'chain solutions' are not seen to stay close to any such typical point with $I \approx D$ for longer time intervals. Instead, we observe a permanent variation of both I and D even during the more quiet time episodes. An attempt to converge a travelling wave solution from nearly recurrent episodes along the 'chain solution' was not successful either. Third, the fact that the period estimated for the 'chain solution' converges to a remarkably robust value after a handful of loops suggests that the shadowed attracting invariant set is indeed a periodic orbit. An attracting heteroclinic cycle has, by definition, an infinite period, but any piecewise continuous, finite-precision approximation to it will possess an 'artificial' period. Though, one should expect that the dynamics of trajectories slow down in the vicinity of a heteroclinic cycle with every loop they spin around and approach the latter [cf. the heteroclinic cycle in $\mathbb{R}^3$ studied by 53] – a behaviour that we do not observe for any of our cases. On the other hand, our observations are in line with the work of Kreilos et al. [54], who successfully isolated a periodic orbit as edge state for an asymptotic suction boundary layer that reveals a structural similarity to the current periodic cycle. The authors provide evidence that the PO emerges from the annihilation of two pairs of fixed points in the context of a saddle-node infinite-period bifurcation, an observation which is of relevance for the ongoing analysis of the presented cases.

Although these arguments provide some evidence that the shadowed relatively attracting cycle is a periodic orbit, none of the above arguments is rigorous enough to conclusively clarify the nature of the attracting invariant set. To close this gap, in the next step one should try to converge the almost recurrent 'chain solutions' to truly periodic orbits with the aid of the Newton-GMRES algorithm. The authors are optimistic that this can be achieved in the near

future for the doubly-symmetric case $\mathrm{PC3200}_{yz}$, taking into account the excellent quality of the initial guess as well as the fact that the flow seems to repeat itself (modulo a rotation by $\pi/2$ about the x-axis) after half the estimated period $T/2 = 281.9T_b$. In case $\mathrm{PC2400}_y$, the situation is more delicate in that the estimated period is too long to be useful as an initial guess for the Newton-GMRES solver, since there is at least one re-iteration of β_i per period necessary to keep the 'chain solution' in the neighbourhood of $\mathscr{M}$. Without further extensions of the numerical approach such as a multipoint shooting technique [e.g. 55] or using an adjointed-based variational Jacobian-free method instead of the Newton-GMRES solver [e.g. 56], there is no hope to converge the current chain solution $\mathrm{PC2400}_y$ to a periodic orbit.

But even without the fully-converged time-recurrent invariant set at hand, the current results open up a new dynamical systems-based perspective on the well-known 'switching' behaviour in square duct flow [12]: Fully-chaotic turbulent trajectories are expected to shadow periodic sets like the ones investigated in the current study for a certain period of their lifetime. During those episodes, they follow a similar dynamics as the invariant sets by which they are attracted and 'switch' from one 'two-wall' state to the other. Note that all detected edge states are purely attracting only within the edge manifold, but are inherently unstable solutions w.r.t. the full phase space. All chaotic trajectories will therefore eventually leave their neighbourhood again and, after a while, will possibly approach and shadow another comparable 'switching' cycle and so on and so forth. In this context, it should be emphasised that the 'switching' between (at least) two alternating flow states is no exclusive feature of the considered symmetric subspaces, but a comparable, though chaotic oscillating dynamics is also visible for edge trajectories in the asymmetric case CA3200, which further underlines the relevance of the current findings for the general, chaotic turbulent case. Further efforts will be made to assess the usefulness of this qualitative phase-space picture of square duct dynamics.

Acknowledgements
This work was supported in part by the European Research Council under the Caust grant ERC-AdG-101018287. In this regard, we want to thank Prof. Javier Jiménez and Dr. Kosuke Osawa for their kind hospitality during the fifth Madrid turbulence summer workshop. We also thank Daniel Morón, Prof. Marc Avila and Prof. Lennaert van Veen for very insightful discussions and their valuable comments on an earlier draft of this manuscript. The simulations were performed on the supercomputer bwUniCluster funded by the Ministry of Science, Research and the Arts Baden-Württemberg and the Universities of the State of Baden-Württemberg. The computer resources, technical expertise and assistance provided by the staff are gratefully acknowledged.

References

[1] Smits A J, McKeon B J and Marusic I 2011 *Ann. Rev. Fluid Mech.* **43** 353–375
[2] Avila M, Barkley D and Hof B 2023 *Ann. Rev. Fluid Mech.* **55** 575–602
[3] Bradshaw P 1987 *Ann. Rev. Fluid Mech.* **19** 53–74
[4] Demuren A O and Rodi W 1984 *J. Fluid Mech.* **140** 189–222
[5] Brundrett E and Baines W D 1964 *J. Fluid Mech.* **19** 375–394
[6] Gessner F B 1973 *J. Fluid Mech.* **58** 1–25
[7] Gavrilakis S 1992 *J. Fluid Mech.* **244** 101–129
[8] Huser A and Biringen S 1993 *J. Fluid Mech.* **257** 65–95
[9] Modesti D, Pirozzoli S, Orlandi P and Grasso F 2018 *J. Fluid Mech.* **847** R1
[10] Sekimoto A, Kawahara G, Sekiyama K, Uhlmann M and Pinelli A 2011 *Phys. Fluids* **23** 075103
[11] Modesti D and Pirozzoli S 2022 *J. Fluid Mech.* **941** A16
[12] Uhlmann M, Pinelli A, Kawahara G and Sekimoto A 2007 *J. Fluid Mech.* **588** 153–162

[13] Pinelli A, Uhlmann M, Sekimoto A and Kawahara G 2010 *J. Fluid Mech.* **644** 107–122
[14] Hamilton J M, Kim J and Waleffe F 1995 *J. Fluid Mech.* **287** 317–348
[15] Waleffe F 1997 *Phys. Fluids* **9** 883–900
[16] Schoppa W and Hussain F 2002 *J. Fluid Mech.* **453** 57–108
[17] Kawahara G and Kamada E 2000 *Trans. Japan Soc. Mech. Eng. B* **66**(643) 89–97
[18] Hopf E 1948 *Comm. Pure Appl. Math.* **1** 303–322
[19] Jiménez J 1987 *CTR Annual Research Briefs* 323–324
[20] Waleffe F 2002 Exact coherent structures and their instabilities: toward a dynamical-system theory of shear turbulence *Proc. Int. Symp. on "Dynamics and Statistics of Coherent Structures in Turbulence: Roles of Elementary Vortices"* ed Kida S (National Center of Sciences, Tokyo, Japan) pp 115–128
[21] Gibson J F, Halcrow J and Cvitanović P 2008 *J. Fluid Mech.* **611** 107–130
[22] Kawahara G, Uhlmann M and van Veen L 2012 *Ann. Rev. Fluid Mech.* **44** 203–225
[23] Graham M D and Floryan D 2021 *Ann. Rev. Fluid Mech.* **53**
[24] Kerswell R R 2005 *Nonlinearity* **18** R17–R44
[25] Wedin H, Bottaro A and Nagata M 2009 *Phys. Rev. E* **79**(6) 065305
[26] Okino S, Nagata M, Wedin H and Bottaro A 2010 *J. Fluid Mech.* **657** 413–429
[27] Okino S and Nagata M 2012 *J. Fluid Mech.* **693** 57–68
[28] Uhlmann M, Kawahara G and Pinelli A 2010 *Phys. Fluids* **22** 084102
[29] Jiménez J and Moin P 1991 *J. Fluid Mech.* **225** 213–240
[30] Guckenheimer J and Holmes P J 1983 *Nonlinear Oscillations, Dynamical Systems, and Bifurcations of Vector Fields* 1st ed (*Applied Mathematical Sciences* vol 42) (Springer)
[31] Wiggins S 2003 *Introduction to Applied Nonlinear Dynamical Systems and Chaos* 2nd ed (*Texts in applied mathematics* vol 2) (Springer-Verlag New York)
[32] Toh S and Itano T 2003 *J. Fluid Mech.* **481** 67–76
[33] Biau D and Bottaro A 2009 *Philos. Trans. R. Soc. A* **367** 529–544
[34] Okino S 2014 Spatially localized solutions in rectangular duct flow *Proc. Fluids Eng. Conf.* (The Japan Society of Mechanical Engineers) p 0802
[35] Avila M, Mellibovsky F, Roland N and Hof B 2013 *Phys. Rev. Lett.* **110**(22) 224502
[36] Haldenwang P, Labrosse G, Abboudi S and Deville M 1984 *J. Comput. Phys.* **55** 115–128
[37] Rai M M and Moin P 1991 *J. Comp. Phys.* **96** 15–53
[38] Verzicco R and Orlandi P 1996 *J. Comput. Phys.* **123** 402–414
[39] Saad Y and Schultz M H 1986 *SIAM J. Scien. Statist. Comp.* **7** 856–869
[40] Trefethen L N and Bau D 1997 *Numerical linear algebra* (*Other titles in applied mathematics* vol 50) (Philadelphia: SIAM)
[41] Chandler G J and Kerswell R R 2013 *J. Fluid Mech.* **722** 554–595
[42] Dennis J E and Schnabel R B 1996 *Numerical Methods for Unconstrained Optimization and Nonlinear Equations* (SIAM)
[43] Viswanath D 2009 *Philos. Trans. R. Soc. A* **367** 561–576
[44] Willis A P 2017 *SoftwareX* **6** 124–127
[45] Duguet Y, Willis A P and Kerswell R R 2008 *J. Fluid Mech.* **613** 255–274
[46] Okino S, Nagata M, Wedin H and Bottaro A 2012 Travelling wave solutions in square duct flow *Progress in Turbulence and Wind Energy IV, Proc. iTi Conf. Turb. 2010* ed Oberlack M, Peinke J, Talamelli A Castillo L and Hölling M (Springer Berlin Heidelberg) pp 135–138
[47] Pringle C C T, Duguet Y and Kerswell R R 2009 *Philos. Trans. R. Soc. A* **367** 457–472
[48] Kawahara G and Kida S 2001 *J. Fluid Mech.* **449** 291–300
[49] Kim H T, Kline S J and Reynolds W C 1971 *J. Fluid Mech.* **50** 133–160

[50] Holmes P, Lumley J L and Berkooz G 1996 *Turbulence, Coherent Structures, Dynamical Systems and Symmetry* 1st ed Cambridge monographs on mechanics (Cambridge Univ. Press)

[51] Aubry N, Holmes P, Lumley J L and Stone E 1988 *J. Fluid Mech.* **192** 115–173

[52] Armbruster D, Guckenheimer J and Holmes P 1988 *Physica D: Nonl. Phen.* **29** 257–282

[53] Guckenheimer J and Holmes P 1988 *Math. Proc. Cambridge Philos. Soc.* **103** 189–192

[54] Kreilos T, Veble G, Schneider T M and Eckhardt B 2013 *J. Fluid Mech.* **726** 100–122

[55] Budanur N B, Short K Y, Farazmand M, Willis A P and Cvitanović P 2017 *J. Fluid Mech.* **833** 274–301

[56] Azimi S, Ashtari O and Schneider T M 2022 *Phys. Rev. E* **105**(1) 014217